Feasibility evaluation of a neutron grating interferometer with an analyzer grating based on a structured scintillator

Youngju Kim, Jongyul Kim, Daeseung Kim, Daniel. S. Hussey, and Seung Wook Lee

Citation: Review of Scientific Instruments **89**, 033701 (2018); doi: 10.1063/1.5009702
View online: https://doi.org/10.1063/1.5009702
View Table of Contents: http://aip.scitation.org/toc/rsi/89/3
Published by the American Institute of Physics

REVIEW OF SCIENTIFIC INSTRUMENTS 89, 033701 (2018)

Feasibility evaluation of a neutron grating interferometer with an analyzer grating based on a structured scintillator

Youngju Kim,[1] Jongyul Kim,[2] Daeseung Kim,[1] Daniel. S. Hussey,[3] and Seung Wook Lee[1,a)]
[1]*School of Mechanical Engineering, Pusan National University, Busan 46241, South Korea*
[2]*Neutron Science Center, Korea Atomic Energy Research Institute, Daejeon 34057, South Korea*
[3]*Neutron Physics Group, National Institute of Standards and Technology, Gaithersburg, Maryland 20899, USA*

(Received 19 October 2017; accepted 2 February 2018; published online 1 March 2018)

We introduce an analyzer grating based on a structured scintillator fabricated by a gadolinium oxysulfide powder filling method for a symmetric Talbot-Lau neutron grating interferometer. This is an alternative way to analyze the Talbot self-image of a grating interferometer without using an absorption grating to block neutrons. Since the structured scintillator analyzer grating itself generates the signal for neutron detection, we do not need an additional scintillator screen as an absorption analyzer grating. We have developed and tested an analyzer grating based on a structured scintillator in our symmetric Talbot-Lau neutron grating interferometer to produce high fidelity absorption, differential phase, and dark-field contrast images. The acquired images have been compared to results of a grating interferometer utilizing a typical absorption analyzer grating with two commercial scintillation screens. The analyzer grating based on the structured scintillator enhances interference fringe visibility and shows a great potential for economical fabrication, compact system design, and so on. We report the performance of the analyzer grating based on a structured scintillator and evaluate its feasibility for the neutron grating interferometer. *Published by AIP Publishing.* https://doi.org/10.1063/1.5009702

I. INTRODUCTION

A grating interferometer provides various information of materials by phase and dark field contrast imaging in addition to conventional attenuation radiography. The use of grating interferometers was revived at synchrotron x-ray facilities,[1,2] and the phase gradient images provided enhanced contrast for low atomic number materials. The predominant geometry was a Talbot interferometer composed of a phase grating which created the near-field diffraction pattern (i.e., the Talbot self-image) and an analyzer grating at the detector to resolve the fine period of the self-image. Due to the intrinsically high transverse coherence of the synchrotron beam, a source grating was unnecessary.

A Talbot-Lau Interferometer (TLI), which introduces a source grating that produces multiple quasi-coherent beams from an incoherent source, is applicable to incoherent radiation such as a laboratory x-ray source.[3,4] With this technological advance, the grating interferometer can be applied to neutron beams; hence, it has been implemented and studied at many neutron research facilities.[5–8]

The use of the neutron grating interferometer mainly focuses on dark field contrast imaging that primarily arises due to small angle neutron scattering. It provides structural information due to the reduction in the interferometer visibility from the dephasing effects of neutron scattering from the micro-inhomogeneity inside an object[9–11] and successfully visualized magnetic domain walls in electrical steel materials using the magnetic property of neutrons.[12–15] In addition, the grating interferometer can be combined with tomography to provide three-dimensional dark field contrast imaging.[11,14,16]

A neutron TLI consists of three gratings as shown in Fig. 1. A source grating G0 is an absorption grating positioned at the neutron beam-defining aperture and creates several spatially quasi-coherent sources to fulfill the initial condition of interference. A phase grating G1 modulates the phase of the neutron beam and creates the Talbot self-image which is an intensity profile that reproduces the periodic structures of the phase grating at the Talbot distance. If the period of the Talbot self-image is below the spatial resolution of a detector, it is not possible to directly resolve the self-image. Thus, an analyzer grating G2 is conventionally installed at the Talbot distance, just in front of the detector.

The TLI has three geometrical configurations depending on the distance between the gratings.[17] The conventional TLI, a common design for neutron sources, has a longer distance between G0 and G1, L, than the distance between G1 and G2, D. If L is the same with D, it is called a symmetric TLI and enables using gratings of identical periods. The symmetric TLI relieves the acute difficulty of fabricating the analyzer grating as the period of G2 is larger, and this is a primary advantage of the symmetric TLI compared to that of the conventional TLI. When L is shorter than D, it is called the inverse TLI. In this geometry, it may be possible to directly resolve the interference pattern by the detector, but the system should be long enough to magnify the interference pattern.

a)Electronic mail: seunglee@pusan.ac.kr

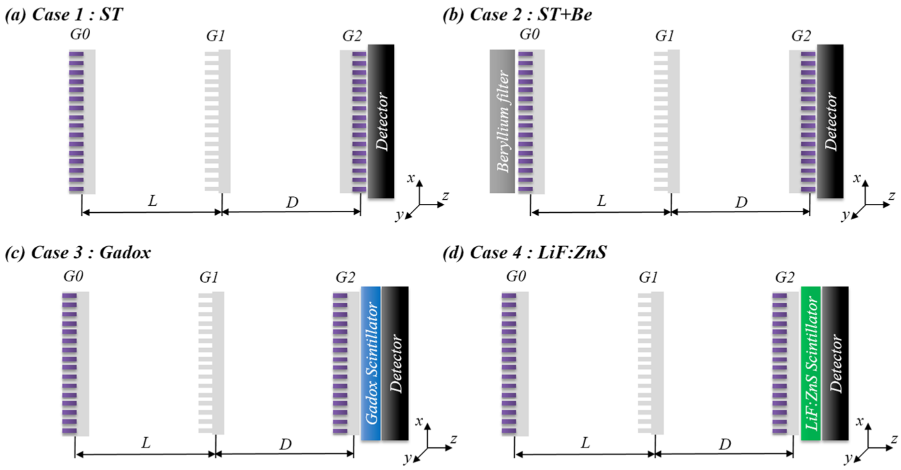

FIG. 1. Schematic configurations of neutron grating interferometers in the experiments. (a) The interferometer is a symmetric TLI, case1, that has a source grating ($G0$), a phase grating ($G1$), and an analyzer grating based on a structured scintillator ($G2$). (b) Case 2 has added a beryllium filter of 5 cm thickness to case 1. (c) Case 3 and (d) case 4 have a Gadox (20 μm thick) and a LiF:ZnS (300 μm thick) scintillator screen behind the analyzer grating, respectively.

Visibility, the amplitude of the moiré pattern, is one of the most important performance metrics of a grating interferometer system.[4] In order to continue to enhance the visibility and reduce the number of components,[18,19] several ideas have appeared such as an embedded x-ray target on which a source grating is patterned[20,21] and a structured scintillator of which the pattern represents that of an analyzer grating. Recently, the visibility of a grating interferometer has been successfully increased by using the structured scintillator in the x-ray imaging field.[22]

In this paper, we describe a neutron grating interferometer with an analyzer grating based on a structured scintillator for increased visibility. The neutron grating interferometer is designed as a symmetric TLI and configured with a one-dimensional line source grating, a two-dimensional checkerboard phase grating, and a two-dimensional mesh grid analyzer grating. The source grating and the analyzer grating are fabricated by the gadolinium oxysulfide powder filling method.[23] The result of the analyzer grating based on the structured scintillator is compared to the results produced by the typical configuration of an absorption grating and scintillator screens of gadolinium oxysulfide and lithium fluoride mixed with zinc sulfide.

II. MATERIALS AND METHODS

The experiments were conducted at the cold neutron imaging beam line NG6 at the NIST Center of Neutron Research (NCNR).[8] Figure 1 shows the schematics of the experimental setups. Cases 1 and 2 used an analyzer grating based on a structured scintillator, and a beryllium filter of 5 cm thickness was additionally installed in case 2. Cases 3 and 4 are typical configurations of an analyzer grating based on an absorption grating with scintillator screens of gadolinium oxysulfide (Gd_2O_2S, Gadox) and lithium fluoride mixed with zinc sulfide (LiF:ZnS), respectively. The detailed information of the interferometer systems used in the experiments is shown in Table I, and the detailed description follows.

All the grating interferometers here have a symmetric TLI geometry which has three gratings with the same period of 50 μm. The source grating was installed in the beam path after the circular beam aperture of 13 mm in diameter and a silicon powder to scatter the beam to increase beam divergence and reduce the flat field structure due to the neutron guide. The analyzer grating based on a structured scintillator was positioned just in front of the detector, and a phase grating was positioned in the middle of the other two gratings. The distance between the gratings, L and D, is 426 cm, which corresponds to a Talbot distance of 3rd order.

The source grating has one-dimensional gadolinium oxysulfide structures filled into the trenches of a silicon substrate; the gadolinium oxysulfide structures have a duty cycle of three quarter, while the silicon structures have a duty cycle of a quarter. The phase grating is a checkerboard type two-dimensional grating with a feature height of 34.39 μm and a duty cycle of a half in Si. The analyzer grating is a mesh grid two-dimensional grating based on a structured scintillator with a duty cycle of a half in gadolinium oxysulfide. Since the source grating has a one-dimensional pattern, the whole system operates in a one-dimensional mode although the phase grating and the analyzer grating have two-dimensional patterns. The phase grating produces a π phase shift at a neutron wavelength of 4.4 Å, and it has the role of generating interference patterns at the Talbot distances in the beam path. The source grating generates one-directional spatial coherence of the beam, and the phase grating produces the self-images. We can approximate the diffraction with the following equation:[24]

TABLE I. Parameters of the grating interferometer systems in the experiments.

Wavelength (Å)	λ	4.4
Inter-grating distance (cm)	G0-G1(L)	426
	G1-G2(D)	426
Period of gratings (μm)	p(p0 = p1 = p2)	50
Height of gratings (μm)	h0	100 (Gadox)
	h1	34.39 (Silicon)
	h2	20 (Gadox)
Duty cycle of gratings	d0	0.75 (Gadox)
	d1	0.5 (Silicon)
	d2	0.5 (Gadox)

$$E(x,y,z) = \exp\left(\frac{2\pi iz}{\lambda}\right)\sum_{m,n} A_{m,n}\exp\left(-i\pi z\lambda\left(\frac{m^2}{{p_x}^2}+\frac{n^2}{{p_y}^2}\right)\right)\exp\left(2\pi i\left(\frac{mx}{p_x}+\frac{ny}{p_y}\right)\right)$$
$$\cong \exp\left(\frac{2\pi iz}{\lambda}\right)\Sigma_m A_m \exp\left(-i\pi z\lambda\frac{m^2}{{p_x}^2}\right)\exp\left(2\pi i\frac{mx}{p_x}\right), \tag{1}$$

where $A_{m,n}$ is the mth and nth Fourier coefficient and p_x and p_y are the grating periods in the x and y directions, respectively. x is the horizontal direction and y is the vertical direction perpendicular to the beam propagation direction z as shown in Fig. 1.

The source grating and the analyzer grating were produced by a gadolinium oxysulfide powder filling method. In this fabrication method, we filled the trenches formed by silicon etching with gadolinium oxysulfide powder mixed with a binding solution and baked it in a furnace to solidify the binding solution. It is simpler and more economical than the conventional grating fabrication processes. Figure 2 shows optical microscopic images of a representative grating to show the fabrication process of the Gadox power filling process. The gratings used in this experiment have been made in the same process, but the design values such as dimensions and shapes are different from the figure. Since gadolinium oxysulfide is a scintillator material, the analyzer grating is straightforwardly employed as a structured scintillator.

The source grating had a gadolinium oxysulfide feature height of 100 μm to provide nearly complete attenuation of the cold neutron beam. As shown in Fig. 1, the analyzer grating here was used in two modes, as a structured scintillator [Figs. 1(a) and 1(b)] or as a typical absorption grating placed in front of a commercial scintillator screen [Figs. 1(c) and 1(d)]. In order to allow the scintillation light to escape, the feature height of the analyzer grating was 20 μm. The stopping power for neutrons with a wavelength of 0.44 nm is about 98%, so this yields an efficient typical absorption grating as well.

Differential phase and dark field contrast images were obtained by phase stepping the source grating in the perpendicular direction of the grating lines.[1,2] The number of phase steps was 8, and they were processed by the Fourier analysis. The exposure time for each configuration was adjusted to produce similar light counts in the detector as shown in Table II. 6 images were merged by a median filter for one phase step image to remove non-statistical noise. The light detector was an Andor sCMOS camera with a 50 mm lens producing 2560×2160 pixel area, and its effective pixel pitch was 51.35 μm.[26]

Figure 3 shows the phantoms used to evaluate imaging performance in the experiments. The step phantom, with 10 steps of 0.5 mm height, was manufactured of copper and brass for absorption and dark field contrast imaging, respectively. The brass alloy was C2680, and its chemical composition by mass is 64% to 68% Cu, 0.07% Pb, 0.05% Fe, and the balance is Zn. The copper of the phantom had pure (99.999%) composition of Cu. The step phantom was positioned 130 mm away from G2. For differential phase contrast imaging, a wedge phantom of a silicon crystal was used and positioned at 530 mm away from the analyzer grating. We placed the wedge phantom farther away from the analyzer grating than the step phantom to obtain high phase sensitivity.[17]

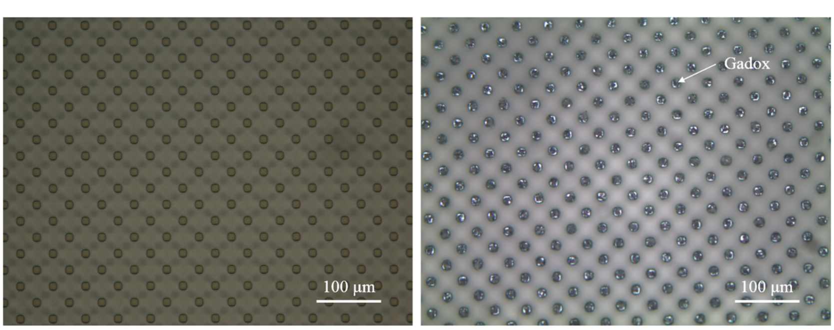

FIG. 2. Optical microscopic images of a representative grating to show the fabrication process of the Gadox filling method. The left one does not have Gadox powder in the silicon trenches. The right one has Gadox powder filled in. (Note: These are photographic images of an example grating to show the fabrication process and are not the real gratings used for this experiment.)

TABLE II. Exposure time and averaged light output in each case. The light output was measured over all the structured area of the grating with a pixel region of interest (ROI) that is (1700×1700) pixels, and the light output has been corrected for the offset signal of detector (dark image).

	Case 1: ST	Case 2: ST + Be	Case 3: Gadox	Case 4: LiF
Exposure time (s)	180	500	15	1.7
Averaged light output (A. U.)	184	236	177	171

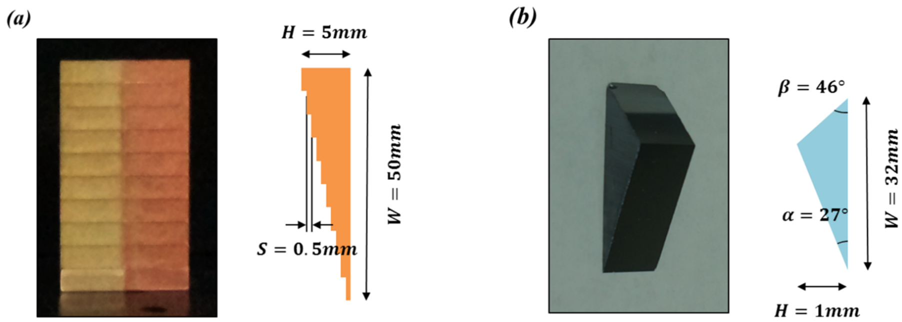

FIG. 3. Phantoms and schematics. (a) Copper and brass steps for absorption and dark field contrast imaging and (b) silicon crystal wedge for differential phase contrast imaging.

III. RESULTS

Table II gives the exposure times for each case to obtain similar average light output except in case 2. In case 2, a beryllium filter of 5 cm thickness cut off the neutron spectrum below a wavelength of about 0.4 nm. As shown in Fig. 4, the visibility in case 2 is higher and the beam profile of the flat field is smoother due to a more narrow spectral width at the expense of reduced light output requiring a factor of 2 increase in exposure time to reach the same light output as in case 1.

The visibility averaged over the reference ROI for case 1-4 is 14.28%, 17.18%, 9.94%, and 10.89%, respectively. The analyzer grating based on a structured scintillator has shown improved visibility for a polychromatic cold neutron beam over the typical configuration. We attribute this improvement to the fact that this combination converts the neutrons only interacting with the patterned scintillators into light signals and passes all the other neutrons through. Moreover, it removes the distance between the two components, thus producing a much clearer moiré pattern for the same level of light output. On the other hand, the typical method as in cases 3 and 4 suffers from the incomplete shielding of the analyzer grating and the inter-distance between the analyzer grating and the scintillator screen, thus producing a degraded moiré pattern and lower visibility.

Figure 5 shows the absorption contrast images of the step phantoms for each case in Fig. 1. Figures 5(e) and 5(f) show the averaged vertical profiles of the absorption contrast over the ROI indicated by the red box for the brass and copper step phantoms. As the step thickness of the phantom increases, the attenuation contrast increases. We have analyzed the resolution for each case. Cases 1 and 2 have coarser resolution than cases

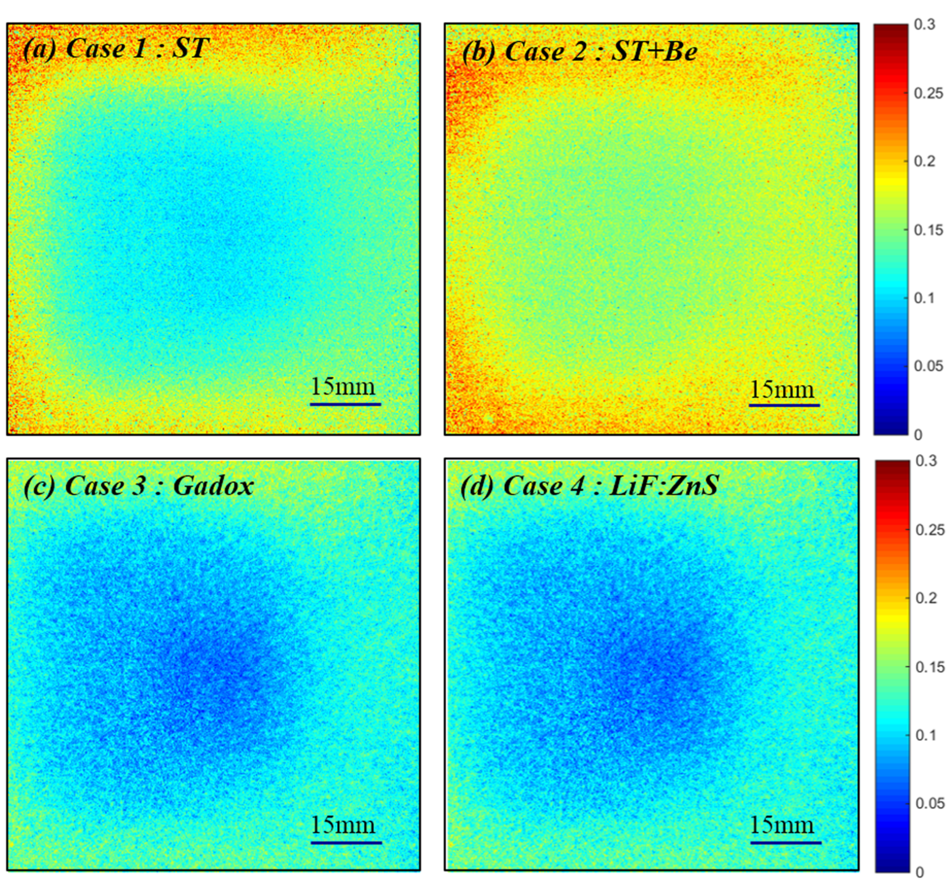

FIG. 4. Visibility map for each case shown in Fig. 1. The average visibilities in the reference ROI (1700 × 1700 pixels) are 14.28%, 17.18%, 9.94%, and 10.89%, respectively.

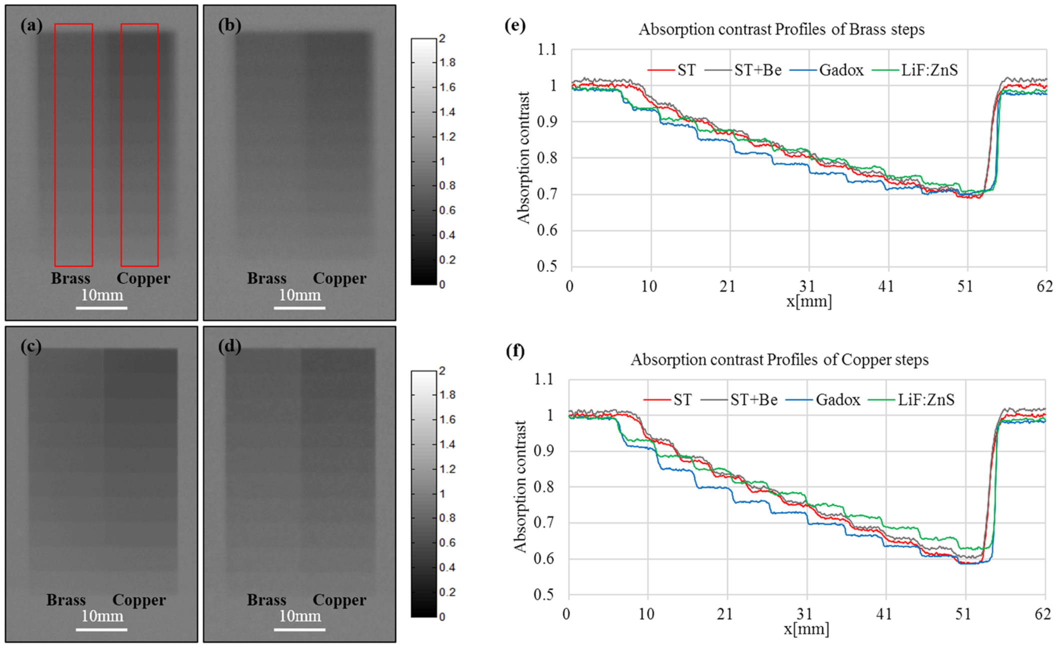

FIG. 5. Absorption contrast images of steps of brass and copper step phantom: (a) case 1: ST, (b) case 2: ST + Be, (c) case 3: Gadox, (d) case 4: LiF:ZnS. Profiles of the absorption images of (e) brass and (f) copper for the four cases.

3 and 4. We can qualitatively see that the resolution for cases 1 and 2 is worse than that for cases 3 and 4 in Figs. 5(a)–5(d). Cases 1 and 2 have smoother profiles at the edges of the step phantom than cases 3 and 4 as shown in Figs. 5(e) and 5(f).

Figure 6 shows the differential phase contrast images and their averaged vertical profiles in the red box area for the four cases. We assess the measurement quality of a differential phase contrast image using the contrast-to-noise ratio (CNR),[25]

$$CNR \propto V\sqrt{\frac{N}{2}}, \tag{2}$$

where V is the visibility and N is the number of photons. According to the equation, the CNR is linearly proportional to the visibility and the square root of the number of photons in the image. Thus, the CNR is poor when the visibility is low and the photon counts are small, and we have found that cases 3 and 4 have worse CNRs as shown in Fig. 6. The CNRs for the four cases have been calculated using the visibility in Fig. 4 and the number of photons in Table II and are 1.5, 1.8, 1.0, and 1.1, respectively. The CNR for case 2 is 1.2 times greater than that for case 1 and about 2 times greater than that for cases 3 and 4. With regard to resolution, cases 1 and 2 have lower resolution than cases 3 and 4 in the same as we have seen in the absorption contrast images.

Figure 7 shows the dark field contrast images and vertical profiles in the red box area of the step phantom for the four cases. The dark field contrast images of the brass phantom show significant contrast due to precipitates of lead and iron in it. The dark field signal of the copper phantom is smaller because there are less scattering elements in it. Since the CNR of the dark field contrast image is the same as that of its corresponding differential phase contrast image, case 2 of the analyzer grating based on a structured scintillator with a beryllium filter shows the best signal contrast. The dark field contrast images for cases 1 and 2 shown in Figs. 7(a) and 7(b) show lower resolution as well as in the differential phase contrast and absorption contrast images.

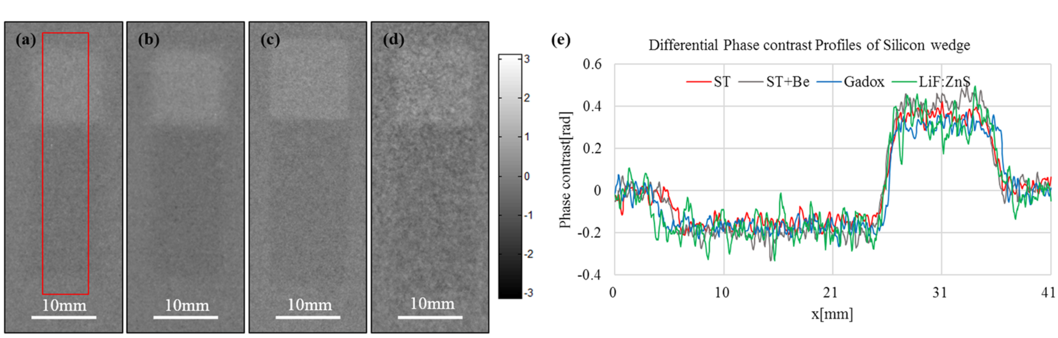

FIG. 6. Differential phase contrast images of a silicon wedge for the four cases: (a) case 1: ST, (b) case 2: ST + Be, (c) case 3: Gadox, (d) case 4: LiF:ZnS. (e) Profiles from the four cases are plotted together.

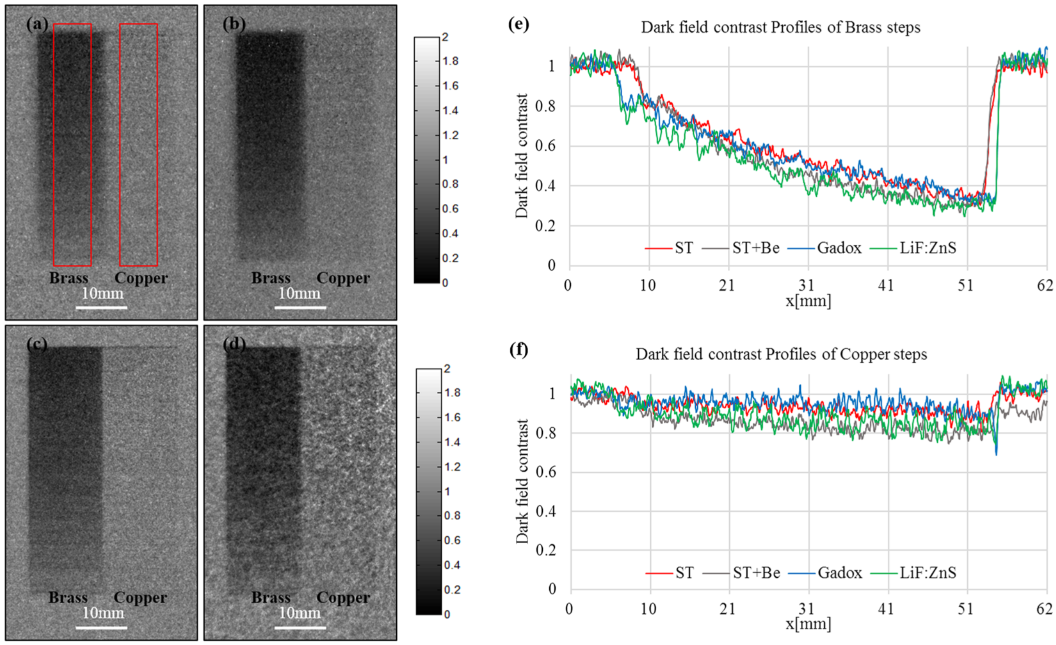

FIG. 7. Dark field images of the brass and copper step phantom: (a) case 1: ST, (b) case 2: ST + Be, (c) case 3: Gadox, (d) case 4: LiF:ZnS. Profiles of the dark field contrast images of (e) brass and (f) copper for the four cases.

IV. DISCUSSION

The neutron grating interferometer using the analyzer grating based on a structured scintillator fabricated by the gadolinium oxysulfide powder filling method has several obvious advantages compared to the typical interferometer using an absorption grating and a scintillator screen separately. The first advantage is an increase in visibility. In the experiments, a visibility of 14% was observed under the condition of a polychromatic cold neutron beam, and the visibility was increased up to 17% when the beryllium filter was used to select lower energy neutrons. The analyzer grating based on a structured scintillator also enables the design of a more compact system. In particular, the grating fabrication method relaxes the difficulty of using Gd metal; it is economical; and it can be used to cover a large field of view (15 cm diameter). Since the analyzer grating based on a structured scintillator lets neutrons pass through the gaps between the structured scintillators while the typical analyzer grating blocks incident neutrons to let passing neutrons interact with a scintillator screen, it can overcome the shadow effect which is a problem in the analyzer grating based on high aspect ratio absorption gratings.

However, as seen from Table II, the analyzer grating based on a structured scintillator requires additional improvements as a scintillator. The exposure time for image acquisition is long due to low light output. It can be used to obtain high visibility in static systems, but in general, a long exposure time is a negative factor. Therefore, production of high light output is fundamentally required. Using a 1D grating system rather than the 2D grating employed here would certainly increase the light output. In addition, we believe that the light output can be improved by a better design of the analyzer grating such as adding reflective coating on a substrate, adopting a transparent scintillator, filling scintillator material into a transparent substrate like quartz, and so on.

Another point that needs to be improved is spatial resolution. All the images produced by the analyzer grating based on a structured scintillator have a degraded edge sharpness compared to images by the typical configuration of an absorption grating and a scintillator screen. It is expected that the spatial resolution will be improved by optimizing materials such as the binding solution used to construct the structured scintillator and especially by reducing the unit size of the 5 μm–15 μm Gadox particles used in these experiments.

V. CONCLUSION

We have evaluated the feasibility of the neutron grating interferometer with the analyzer grating based on a structured scintillator fabricated by the gadolinium oxysulfide powder filling method. It has successfully provided absorption, differential phase, and dark field contrast images. The visibility of the grating interferometer with the grating was better than that with the conventional absorption grating combined with a scintillation screen, and the highest visibility achieved was 17% when it was tested with a polychromatic cold neutron beam filtered by a beryllium filter. The higher visibility when using the analyzer grating with a structured scintillator has improved the CNR, but the resolution was no better than that with the conventional one. However, it is necessary to improve the light output and image resolution through further studies. We believe that these further improvements in light output and image resolution will produce a superior symmetric Talbot-Lau interferometer.

ACKNOWLEDGMENTS

This work was supported by the National R&D (Nos. NRF-2014R1A1A2056795 and NRF-2017K1A3A7A09016

309) and the Radiation Technology R&D (No. NRF-2017M2A2A6A01016849) program through the National Research Foundation of Korea funded by the Ministry of Science, ICT & Future Planning and by the U.S. Department of Commerce, the NIST Radiation and Physics Division, the Director's office of NIST, the NIST Center for Neutron Research.

[1]A. Momose, Opt. Express **11**, 2303 (2003).
[2]T. Weitkamp, A. Diaz, C. David, F. Pfeiffer, M. Stampanoni, P. Cloetens, and E. Ziegler, Opt. Express **13**, 6296 (2005).
[3]F. Pfeiffer, T. Weitkamp, O. Bunk, and C. David, Nat. Phys. **2**, 258 (2006).
[4]F. Pfeiffer, M. Bech, O. Bunk, P. Kraft, E. F. Eikenberry, C. Brönnimann, C. Grünzweig, and C. David, Nat. Mater. **7**, 134 (2008).
[5]S. W. Lee, D. S. Hussey, D. L. Jacobson, C. M. Sim, and M. Arif, Nucl. Instrum. Methods Phys. Res., Sect. A **605**, 16 (2009).
[6]S. W. Lee, Y. K. Jun, and O. Y. Kwon, J. Korean Phys. Soc. **58**, 730 (2011).
[7]A. P. Kaestner, S. Hartmann, G. Kühne, G. Frei, C. Grünzweig, L. Josic, F. Schmid, and E. H. Lehmann, Nucl. Instrum. Methods Phys. Res., Sect. A **659**, 387 (2011).
[8]D. S. Hussey, C. Brocker, J. C. Cook, D. L. Jacobson, T. R. Gentile, W. C. Chen, E. Baltic, D. V. Baxter, J. Doskow, and M. Arif, Phys. Procedia **69**, 48 (2015).
[9]C. Grünzweig, J. Kopecek, B. Betz, A. Kaestner, K. Jefimovs, J. Kohlbrecher, U. Gasser, O. Bunk, C. David, E. Lehmann, T. Donath, and F. Pfeiffer, Phys. Rev. B **88**, 125104 (2013).
[10]A. Hilger, N. Kardjilov, T. Kandemir, I. Manke, J. Banhart, D. Penumadu, A. Manescu, and M. Strobl, J. Appl. Phys. **107**, 036101 (2010).
[11]F. Pfeiffer, C. Grünzweig, O. Bunk, G. Frei, E. Lehmann, and C. David, Phys. Rev. Lett. **96**, 215505 (2006).
[12]C. Grünzweig, C. David, O. Bunk, M. Dierolf, G. Frei, G. Kühne, R. Schäfer, S. Pofahl, H. M. R. Rønnow, and F. Pfeiffer, Appl. Phys. Lett. **93**, 112504 (2008).
[13]S. W. Lee, K. Y. Kim, O. Y. Kwon, N. Kardjilov, M. Dawson, A. Hilger, and I. Manke, Appl. Phys. Express **3**, 106602 (2010).
[14]I. Manke, N. Kardjilov, R. Schäfer, A. Hilger, M. Strobl, M. Dawson, C. Grünzweig, G. Behr, M. Hentschel, C. David, A. Kupsch, A. Lange, and J. Banhart, Nat. Commun. **1**, 125 (2010).
[15]C. Grünzweig, C. David, O. Bunk, M. Dierolf, G. Frei, G. Kuhne, J. Kohlbrecher, R. Schäfer, P. Lejcek, H. M. R. Rønnow, and F. Pfeiffer, Phys. Rev. Lett. **101**, 025504 (2008).
[16]M. Strobl, C. Grünzweig, A. Hilger, I. Manke, N. Kardjilov, C. David, and F. Pfeiffer, Phys. Rev. Lett. **101**, 123902 (2008).
[17]T. Donath, M. Chabior, F. Pfeiffer, O. Bunk, E. Reznikova, J. Mohr, E. Hempel, S. Popescu, M. Hoheisel, M. Schuster, J. Baumann, and C. David, J. Appl. Phys. **106**, 054703 (2009).
[18]G. Sato, T. Kondoh, H. Itoh, S. Handa, K. Yamaguchi, T. Nakamura, K. Nagai, C. Ouchi, T. Teshima, Y. Setomoto, and T. Den, Opt. Lett. **36**, 3551 (2011).
[19]C. Grünzweig, F. Pfeiffer, O. Bunk, T. Donath, G. Kühne, G. Frei, M. Dierolf, and C. David, Rev. Sci. Instrum. **79**, 053703 (2008).
[20]N. Morimoto, S. Fujino, K. Ohshima, J. Harada, T. Hosoi, H. Watanabe, and T. Shimura, Opt. Lett. **39**, 4297 (2014).
[21]N. Morimoto, S. Fujino, A. Yamazaki, Y. Ito, T. Hosoi, H. Watanabe, and T. Shimura, Opt. Express **23**, 16582 (2015).
[22]S. Rutishauser, I. Zanette, T. Donath, A. Sahlholm, J. Linnros, and C. David, Appl. Phys. Lett. **98**, 171107 (2011).
[23]J. Kim, K. H. Lee, C. H. Lim, T. Kim, C. W. Ahn, G. Cho, and S. W. Lee, Rev. Sci. Instrum. **84**, 063705 (2013).
[24]M. Jiang, C. L. Wyatt, and G. Wang, Int. J. Biomed. Imaging **2008**, 827152.
[25]K. Engel, D. Geller, T. Köhler, G. Martens, S. Schusser, G. Vogtmeier, and E. Rössl, Nucl. Instrum. Methods Phys. Res., Sect. A **648**, S202 (2011).
[26]Certain trade names and company products are mentioned in the text or identified in an illustration in order to adequately specify the experimental procedure and equipment used. In neither case does such identification imply recommendation or endorsement by the National Institute of Standards and Technology nor does it imply that the products are necessarily the best available for the purpose.